Monthly Notices of the ROYAL ASTRONOMICAL SOCIETY

MNRAS **471,** 2902–2916 (2017) doi:10.1093/mnras/stx1560

# Multiband study of RX J0838−2827 and XMM J083850.4−282759: a new asynchronous magnetic cataclysmic variable and a candidate transitional millisecond pulsar

N. Rea,[1,2]★ F. Coti Zelati,[1,2,3,4] P. Esposito,[2] P. D'Avanzo,[4] D. de Martino,[5] G. L. Israel,[6] D. F. Torres,[1,7] S. Campana,[4] T. M. Belloni,[4] A. Papitto,[6] N. Masetti,[8,9] L. Carrasco,[10] A. Possenti,[11] M. Wieringa,[12] E. De Oña Wilhelmi,[1] J. Li,[1] E. Bozzo,[13] C. Ferrigno,[13] M. Linares,[14,15,16] T. M. Tauris,[17,18] M. Hernanz,[1] I. Ribas,[1] M. Monelli,[14,15] A. Borghese,[2] M. C. Baglio[3,4] and J. Casares[14,15,19]

*Affiliations are listed at the end of the paper*

Accepted 2017 June 20. Received 2017 June 19; in original form 2016 November 10

**ABSTRACT**

In a search for the counterpart to the *Fermi*-LAT source 3FGL J0838.8−2829, we performed a multiwavelength campaign: in the X-ray band with *Swift* and *XMM–Newton*; in the infrared and optical with OAGH, ESO-NTT and IAC80; and in the radio with ATCA observations. We also used archival hard X-ray data obtained by *INTEGRAL*. We report on three X-ray sources consistent with the position of the *Fermi*-LAT source. We confirm the identification of the brightest object, RX J0838−2827, as a magnetic cataclysmic variable that we recognize as an asynchronous system (not associated with the *Fermi*-LAT source). RX J0838−2827 is extremely variable in the X-ray and optical bands, and timing analysis reveals the presence of several periodicities modulating its X-ray and optical emission. The most evident modulations are interpreted as being caused by the binary system orbital period of ∼1.64 h and the white dwarf spin period of ∼1.47 h. A strong flux modulation at ∼15 h is observed at all energy bands, consistent with the beat frequency between spin and orbital periods. Optical spectra show prominent H$\beta$, He I and He II emission lines that are Doppler-modulated at the orbital period and at the beat period. Therefore, RX J0838−2827 accretes through a disc-less configuration and could be either a strongly asynchronous polar or a rare example of a pre-polar system on its way to reaching synchronism. Regarding the other two X-ray sources, XMM J083850.4−282759 showed a variable X-ray emission, with a powerful flare lasting for ∼600 s, similar to what is observed in transitional millisecond pulsars during the subluminous disc state: this observation possibly means that this source can be associated with the *Fermi*-LAT source.

**Key words:** accretion, accretion discs – novae, cataclysmic variables – pulsars: general – white dwarfs – X-rays: individual: RX J0838−2827– X-rays: individual: XMM J083850.4−282759.

## 1 INTRODUCTION

### 1.1 Cataclysmic variables

Cataclysmic variables (hereafter CVs) are close binary systems hosting a white dwarf (WD) and a low-mass main sequence star that typically fills its Roche lobe and is transferring material towards the compact object (see Warner 2003 for a review). About 20–25 per cent of the known CVs harbour WDs with magnetic fields in the range $10^5$–$10^8$ G and are known as magnetic CVs (mCVs; Ferrario, de Martino & Gänsicke 2015). These mCVs can be divided into two main groups: the intermediate polars (IPs) and the polars. The former are characterized by asynchronously rotating WDs ($P_{\rm spin} \ll P_{\rm orb}$) with spin periods ranging from a few hundreds to thousands of seconds, and orbital periods from one to tens of hours; typically, they accrete via a truncated accretion disc. Owing to the lack of synchronisation and of optical/near-infrared circular

★ E-mail: rea@ice.csic.es

polarization, the WD is believed to possess moderately low magnetic fields ($\leq 10^7$ G). The polars, on the other hand, consist of orbitally locked rotating WDs ($P_{\rm spin} = P_{\rm orb} \sim$ hours) and are circularly polarized in the optical/near-infrared (see Cropper 1990). Their magnetic field as measured from cyclotron emission is in the range ∼10–300 MG, preventing the formation of an accretion disc; thus, accretion proceeds directly from the donor star on to the WD magnetic poles through a stream.

A handful of polars have been found to be slightly desynchronized (≤2 per cent), namely V1500 Cyg, BY Cam, V1432 Aql and CD Ind (Campbell & Schwope 1999). Another candidate, SWIFT J2319.4+2619, was discovered recently (Shafter et al. 2008). Since V1500 Cyg exploded as a nova in 1975, these asynchronous polars are believed to have undergone a nova explosion in the past and they will return to synchronism in hundreds of years (Boyd et al. 2014; Harrison & Campbell 2016). However, only V1500 Cyg is known to be a nova, and searches for nova shells did not result in any detections (Pagnotta & Zurek 2016).

Recently, two systems were found to be desynchronized at a much higher level (i.e. ≫2 per cent), namely Paloma (Schwarz et al. 2007) and IGR J19552+0044 (Bernardini et al. 2013). These systems might be regarded either as IPs with a very low degree of asynchronism or as polars with a large degree of asynchronism. In the former case these systems are not expected to reach synchronism, while in the latter case they may represent the true polar progenitors (see Norton, Wynn & Somerscales 2004). Despite their small number, asynchronous polars represent excellent laboratories for the study of the physics of mass transfer in the case of a varying magnetic field geometry, especially because of the continuous changes of orientation between the WD magnetic field axis and the accretion flow.

### 1.2 Transitional millisecond pulsars

The short spin periods of binary millisecond pulsars are the outcome of the accretion onto the neutron star (NS) of the mass transferred by a low-mass late-type companion star through an accretion disc (Alpar et al. 1982). After a Gyr-long mass accretion phase during which the binary system shines as a bright low-mass X-ray binary (NS-LMXB), the mass transfer rate decreases, allowing the activation of a – now rapidly spinning – radio/gamma-ray millisecond pulsar (MSP), powered by the rotation of its magnetic field. The tight association between radio MSPs and NS-LMXBs has recently been demonstrated by the discovery of three transitional millisecond pulsars (PSR J1023+0038, Archibald et al. 2009; IGR J18245−2452 in the globular cluster M28, Papitto et al. 2013; XSS J12270−4859, Bassa et al. 2014 de Martino et al. 2014;).

These sources have been observed to switch between accretion- and rotation-powered emission on time-scales ranging from a couple of weeks to months, showing that such state transitions may take place on time-scales compatible with those of the variations of the mass accretion rate onto the NS. At high mass inflow rates, the radio pulsar is shut off and the system is bright in the X-ray ($L_{\rm X} > 10^{36}$ erg s$^{-1}$). At low mass inflow rates, the magnetosphere expands up to the light cylinder, activating the radio pulsar. The disc disappears and the system is faint in the X-ray ($L_{\rm X} \sim 10^{32}$ erg s$^{-1}$).

Surprisingly, in addition to the X-ray outburst accreting state and the radio pulsar state, the three known transitional MSPs have been observed in another extremely peculiar *subluminous* disc state, with $L_{\rm X} \sim 10^{33}$ erg s$^{-1}$ (see also Linares 2014). During this state, both PSR J1023+0038 (Archibald et al. 2015) and XSS J1227−4859 (Papitto et al. 2015) showed evidence that part of the disc material was being accreted onto the NS surface. These subluminous states were accompanied by X-ray flaring activity, a sizeable gamma-ray emission and a flat radio spectrum. These phenomena are typical jet signatures in accreting compact objects, suggesting that large mass outflows could be launched by the rapidly rotating propellering magnetosphere of these pulsars (Papitto, Torres & Li 2014; Papitto & Torres 2015; but see also Takata et al. 2014 for an alternative modelling based on a pulsar wind/disc shock).

### 1.3 The *ROSAT* source: 1RXS J083842.1−282723

1RXS J083842.1−282723 (RX J0838−2827 hereafter) was discovered by *ROSAT*, and tentatively classified as a CV by Masetti et al. (2013) based on Balmer and helium emission lines observed in its optical spectrum. Because two of the three transitional MSPs were formerly misclassified as CVs because of their CV-like optical spectra, searches within the error circles of newly discovered but still unidentified *Fermi*-LAT sources are being carried out, despite early tentative classifications based on optical spectroscopy. In particular, the spatial coincidence with the unidentified gamma-ray source 3FGL J0838.8−2829 in the *Fermi* Large Area Telescope (LAT) four-year point-source catalogue (Acero et al. 2015) and the variability of the X-ray emission detected on a time-scale of a few hours in archival *Swift* observations made the nature of the source controversial.

We report in this paper on a large unprecedented multi-band campaign of the field of 3FGL J0838.8−2829 in the radio, infrared, optical and X-ray bands. In Sections 2, 3 and 4, we report on the details of the observations of the field of 3FGL J0838.8−2829. In Section 5, we present the data analysis and results on RX J0838−2827. In Section 6, we report on the analysis of the other X-ray sources associated with 3FGL J0838.8−2829 and in particular on the flaring source XMM J083850.4−282759, which might be a new transitional millisecond pulsar possibly associated with the gamma-ray emission. A discussion follows in Section 7.

## 2 X-RAY OBSERVATIONS

We report here and in the following few sections on the multi-band data analysis of and results for RX J0838−2827, while in Section 6 we report on the other X-ray sources in the field, in particular on the flaring X-ray source XMM J083850.4−282759.

### 2.1 *XMM–Newton*

Two *XMM–Newton* observations were carried out, on 2015 October 20–21 (ID: 0764420101; PI: Rea) and December 2–3 (ID: 0790180101; thanks to *XMM* Director's Time), and in both cases RX J0838−2827 was placed at the aim point of the European Photon Imaging Cameras (EPIC). The pn camera (Strüder et al. 2001) was configured in large-window mode (LW; 47.7-ms time resolution), whereas the two MOS cameras (Turner et al. 2001) were operated in small-window mode (SW; 0.3-s time resolution). The thin optical blocking filter was positioned in front of the cameras in both observations. The reflection grating spectrometers (RGS; den Herder et al. 2001) were operated in standard spectroscopy mode. The journal of the two observations is reported in Table 1.

#### 2.1.1 *EPIC data*

We processed the raw observation data files using the EPPROC (for pn data) and EMPROC (for MOS data) tasks of the *XMM–Newton* Science

**Table 1.** Log of the X-ray observations.

| Satellite | Obs. ID | Date (YY/MM/DD) | Start – End time of exposure (MJD) | Instrument | Mode | Exposure[a] (ks) | RX J0838−2827 count rate[b] (counts $s^{-1}$) |
|---|---|---|---|---|---|---|---|
| *XMM–Newton* | 0764420101 | 2015/10/20-21 | 57 315.4250 – 57 316.0116 | EPIC pn | LW | 47.2 | $2.053 \pm 0.007$ |
| | | | | EPIC MOS 1 | SW | 51.1 | $0.5957 \pm 0.0004$ |
| | | | | EPIC MOS 2 | SW | 51.0 | $0.5743 \pm 0.0003$ |
| | | | | RGS 1 | spectroscopy | 52.7 | $0.0447 \pm 0.0007$ |
| | | | | RGS 2 | spectroscopy | 52.8 | $0.0456 \pm 0.0008$ |
| *XMM–Newton* | 0790180101 | 2015/12/02-03 | 57 358.9411 – 57 359.8111 | EPIC pn | LW | 69.1 | $1.714 \pm 0.007$ |
| | | | | EPIC MOS 1 | SW | 74.0 | $0.529 \pm 0.003$ |
| | | | | EPIC MOS 2 | SW | 74.0 | $0.533 \pm 0.003$ |
| | | | | RGS 1 | spectroscopy | 76.3 | $0.0422 \pm 0.0005$ |
| | | | | RGS 2 | spectroscopy | 76.4 | $0.0429 \pm 0.0007$ |
| *Swift* | 00041343002 | 2010/10/02 | 55 471.7469 – 55 471.9604 | XRT | PC | 4.1 | $0.086 \pm 0.005$ |
| | 00046948001 | 2011/12/18 | 55 913.4285 – 55 913.5048 | XRT | PC | 2.0 | $0.074 \pm 0.006$ |
| | 00046948002 | 2014/10/07 | 56 937.9180 – 56 937.9999 | XRT | PC | 3.0 | $0.069 \pm 0.005$ |
| | 00046948003 | 2014/10/11 | 56 941.3212 – 56 941.8555 | XRT | PC | 2.6 | $0.061 \pm 0.005$ |
| | 00046948004 | 2014/10/15 | 56 945.1198 – 56 945.5923 | XRT | PC | 2.7 | $0.082 \pm 0.006$ |
| | 00046948005 | 2014/10/19 | 56 949.2479 – 56 949.7930 | XRT | PC | 2.5 | $0.127 \pm 0.007$ |
| | 00041343003 | 2015/10/14 | 57 309.4321 – 57 309.5680 | XRT | PC | 2.0 | $0.18 \pm 0.01$ |
| | 00041343004 | 2015/12/27-28 | 57 383.0380 – 57 384.1743 | XRT | WT | 10.4 | $0.217 \pm 0.005$ |
| | 00041343005 | 2015/12/31 | 57 387.4330 – 57 387.6291 | XRT | WT | 1.4 | $0.37 \pm 0.02$ |
| | 00046948006 | 2016/01/12 | 57 399.0082 – 57 399.7305 | XRT | WT | 4.0 | $0.312 \pm 0.009$ |
| | 00046948007 | 2016/01/13 | 57 400.0037 – 57 400.5470 | XRT | WT | 0.5 | $0.13 \pm 0.02$ |
| | 00046948008 | 2016/01/14 | 57 401.0678 – 57 402.0000 | XRT | WT | 3.5 | $0.151 \pm 0.007$ |
| | 00046948009 | 2016/01/17 | 57 404.3239 – 57 404.6413 | XRT | WT | 2.8 | $0.157 \pm 0.008$ |
| | 00046948010 | 2016/01/20 | 57 407.3096 – 57 407.8395 | XRT | WT | 3.7 | $0.190 \pm 0.008$ |

*Notes*. [a]Dead-time-corrected on-source exposure.
[b]Average background-subtracted count rate in the 0.2–10 keV energy band for the EPIC instruments, in the 0.35–2.5 keV energy band for the combined RGS first-order data sets, and in the 0.3–10 keV energy band for the *Swift* XRT data.

Analysis System (SAS,[1] version 15.0), with the calibration files in the data base released in 2016 January (XMM-CCF-REL-332).

The inspection of the EPIC light-curves binned at 10 s revealed episodes of strong flaring particle background in both observations. For the spatial and spectral analysis, we discarded the intervals affected by the flaring background, which were pinpointed by applying intensity filters on the light-curves, following the procedure described by De Luca & Molendi (2004). This reduced the effective exposure time to approximately 38.9 (pn), 48.5 (MOS 1) and 48.4 (MOS 2) ks for the first observation, and to 64.6 (pn), 71.5 (MOS 1) and 71.2 (MOS 2) ks for the second observation.

We ran the SAS source detection script EDETECT_CHAIN on the combined event lists from the two observations. This returned for RX J0838−2827 the position RA = $08^{h}38^{m}43^{s}.20$, Dec.= $-28^{\circ}27'01''.44$ (J2000.0), with an uncertainty of 1.4 arcsec (radius, at the 90 per cent confidence level).[2] This is fully consistent with the more accurate position of the optical counterpart, RA = $08^{h}38^{m}43^{s}.37$, Dec.= $-28^{\circ}27'01''.5$, with an uncertainty of about 0.2 arcsec (Masetti et al. 2013). The 0.2–10 keV image of the field of 3FGL J0838.8−2829 is shown in Fig. 1, and RX J0838−2827's light-curves are shown in in Fig. 2. It was created by stacking the images of the EPIC cameras cleaned from bad pixels and hot columns from both observations. Apart from RX J0838−2827, two other X-ray sources were identified in the 68 per cent error circle of 3FGL J0838.8−2829. In the following we will term them XMM J083850.4−282759 and XMM J083842.7−283832 (see Table 4 for details of their positions and X-ray properties).

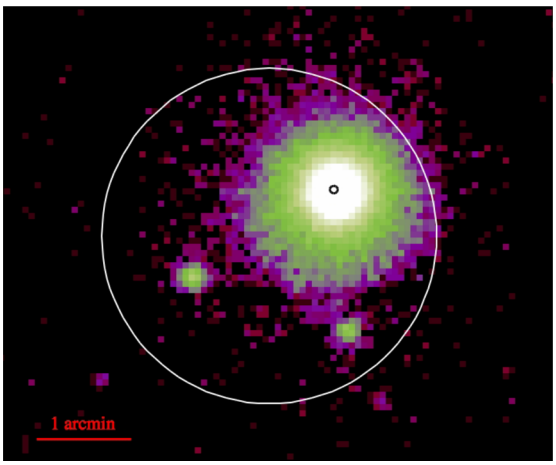


**Figure 1.** Field around RX J0838−2827 in the 0.2–10 keV band as observed by *XMM–Newton*. The image shows the merging of all observations and data from EPIC instruments, for a total exposure time of ∼125 ks. The white circle shows the position of the Fermi-LAT source 3FGL J0838.8−2829 with a $0.^{\circ}03$ error radius (at the 68 per cent confidence level) as reported in the 3FGL catalogue. The black circle is centred on the best optical position, with an error circle of 2 arcsec (increasing the optical positional accuracy by a factor of 10 for imaging purposes). North is up, and east is left.

For the study of RX J0838−2827, we collected the source counts within a circle with a radius of 40 arcsec for the pn data, and of 30 arcsec for the MOS data. The background was extracted from

[1] See http://xmm.esac.esa.int/sas/
[2] The uncertainty on the position is evaluated as the quadratic sum of the statistical uncertainty given by the task EDETECT_CHAIN and the systematic absolute pointing uncertainty of *XMM–Newton*.

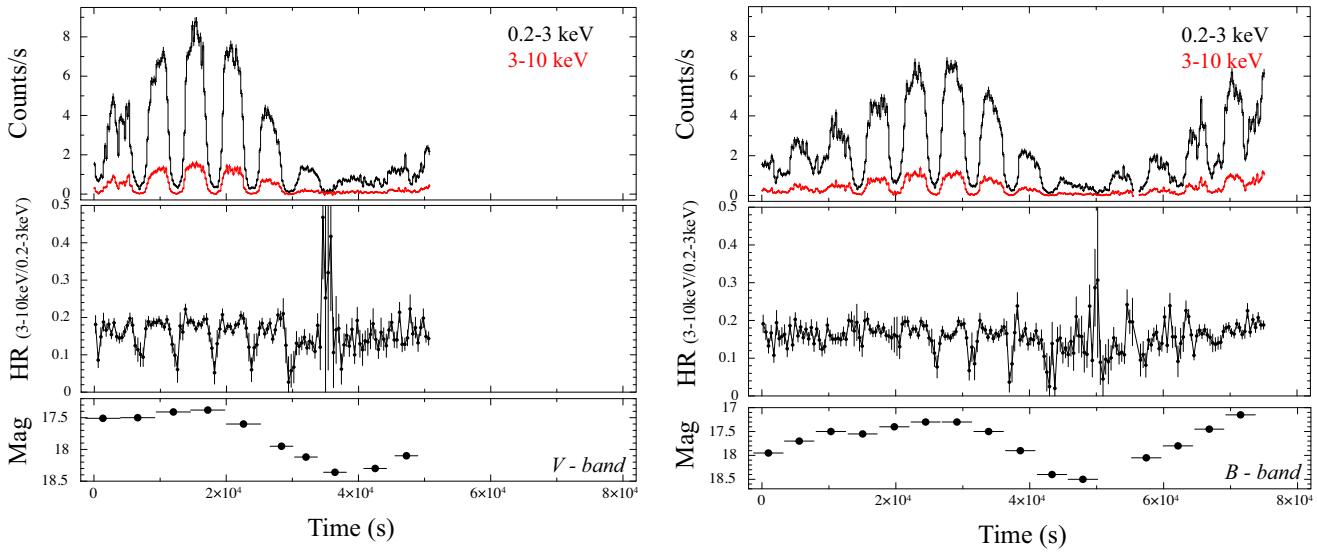


**Figure 2.** *XMM–Newton* EPIC (pn+MOS) light-curves (with a binning time of 200 s) of RX J0838−2827 in two energy bands (and hardness ratios) for the first (left) and second (right) *XMM–Newton* observations. The bottom panels show the *XMM–Newton* optical monitor magnitudes during the two observations (see text for details). Errors are smaller than the markers (∼0.02–0.04 mag).

circles located on the same CCD as the source (so as to guarantee similar low-energy noise subtraction) and avoiding detector areas contaminated by possible out-of-time events from the source (in the pn) or too near to the CCD edges. In contrast, data products for the other two sources were extracted only from the event lists of the pn, because both fell outside the central window of the MOS instruments.

We restricted the analysis to photons in the 0.2–10 keV energy range with PATTERN ≤4 for the pn and ≤12 for the MOS, and FLAG = 0 (we also checked that the data were not affected by pile-up). For the spectral analysis of RX J0838−2827 we used only the data acquired by the pn camera, which provides the spectra with the highest counting statistics, in order to avoid systematic errors introduced by cross-calibration uncertainties (we checked that the MOS spectra were in agreement with the results from the pn camera). We generated the spectral redistribution matrices and ancillary response files for each of the three sources with the RMFGEN and ARFGEN tools, respectively. The fits were performed with the XSPEC package (version 12.9.0; Arnaud 1996), using $\chi^2$ statistics. For the timing analysis, we converted the photon arrival times to the Solar system barycentre reference frame using the SAS task BARYCEN and the DE-200 Solar system ephemeris.

### 2.1.2 *RGS data*

We processed the data using the task RGSPROC of SAS in order to produce calibrated and concatenated photon event lists, spectra and response matrices. We focused our analysis on the first-order spectra alone, which are the best calibrated and have a higher number of counts. First, we subtracted the model background spectra, which were created by the standard RGS pipeline and are template background files based on the count rate in CCD 9. We then combined the spectra using RGSCOMBINE, which appropriately accounts for the response matrices and backgrounds of the different spectrometers, and rebinned the resulting spectra to have at least one count per energy bin. The analysis was limited to the energy interval 0.35–2.5 keV (5–38 Å), where the calibration of the response is most accurate (see Fig. 3).

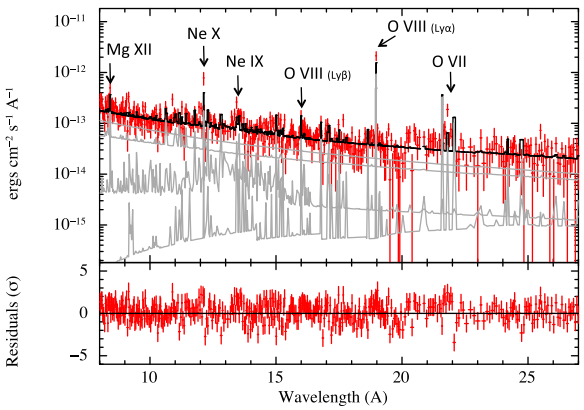


**Figure 3.** *XMM–Newton* RGS first-order spectra of RX J0838−2827 for the second observation. Grey lines represent the three ionized plasma components of the model (black line) that best fits the pn (and RGS) data.

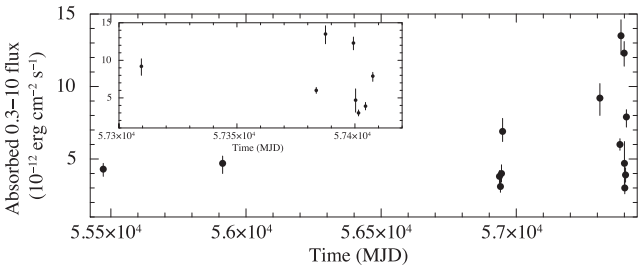


**Figure 4.** *Swift* XRT long-term light-curve of RX J0838−2827. Fluxes relative to the most recent observations are shown in the inset.

## 2.2 *Swift* X-ray telescope

The X-ray telescope (XRT; Burrows et al. 2005) onboard the *Swift* satellite observed the field of RX J0838−2827 for a total of 14 times between 2010 September 8 and 2016 January 20 (see Table 1 for a log of the observations, and Fig. 4). The first seven observations were carried out in the photon-counting (PC) mode, which provides

a two-dimensional image and a time resolution of 2.5073 s. The last seven observations were instead performed in windowed timing (WT) mode; that is, data were transferred from the imaging array to the frame store array with an integration time of 1.78 ms, at the expense of one dimension of spatial resolution (see Hill et al. 2004 for a detailed description of the XRT readout modes).

The data were analysed primarily to study the X-ray long-term variability of RX J0838−2827. We processed the data with standard screening criteria and generated exposure maps with the task XRTPIPELINE (version 0.13.2) from the FTOOLS package (Blackburn 1995), using the optical position of the source (Masetti et al. 2013) and the spacecraft attitude file. We selected events with grades 0–12 and 0 for the PC and WT data, respectively, and extracted the source and background spectra using XSELECT (version 2.4). We accumulated the source counts from a circular region with a radius of 20 pixels (one XRT pixel corresponds to about 2.36 arcsec). In order to estimate the background in the PC-mode data, we extracted the events within an annulus centred on the source position with an inner and an outer radius of 40 and 80 pixels, respectively. For the WT-mode data, we opted for a circle far from the target and of the same size as the source circle, owing to the small extent of the WT window.

We created the observation-specific ancillary response files (using exposure maps) with XRTMKARF (version 0.6.3), which corrects for the loss of counts owing to hot columns and bad pixels, and accounts for different extraction regions, telescope vignetting and point spread function (PSF) corrections. We then assigned the appropriate redistribution matrix available in the HEASARC calibration data base,[3] excluded bad spectral channels, and grouped the background-subtracted spectra to have at least 20 counts in each spectral bin. We limited the spectral analysis to the energy range 0.3–10 keV for PC-mode data and to 0.7–10 keV for the WT-mode data, owing to known calibration issues in WT that result in spurious bumps and/or turn-ups in the spectra at low energies.[4]

### 2.3 *INTEGRAL*

We analysed all publicly available *INTEGRAL* data collected in the direction of the source in the past 13 yr of the mission. We considered all *INTEGRAL* science windows (ScW), namely the various pointings each lasting ∼2–3 ks, in which the source was observed within 12° off-axis from the satellite aim point for the IBIS/ISGRI instrument (Lebrun et al. 2003; Ubertini et al. 2003) and 3°.5 off-axis for the two JEM-X instruments (Lund et al. 2003). All data were processed and analysed using the Off-line Scientific Analysis software (OSA) version 10.2 distributed by the ISDC (Courvoisier et al. 2003).

We found that the region around 3FGL J0838.8−2829 was probed by *INTEGRAL* for a total of 892 ks effective exposure with IBIS/ISGRI, and for 15.5 ks (10.0 ks) with JEM-X1 (JEM-X2). The data set spanned from satellite revolution 28 (starting on 52644 MJD) to 1625 (ending on 57381 MJD). We built the IBIS/ISGRI mosaics in the 20–40 keV and 40–80 keV energy bands, and the JEM-X mosaics in the 3–10 keV energy band. RX J0838−2827 was not detected by these instruments. Using the OSA MOSAIC_SPEC tool we estimated a $3\sigma$ upper limit on the source hard X-ray flux of 1 mCrab ($\sim 8 \times 10^{-12}$ erg cm$^{-2}$ s$^{-1}$) in the 20–40 keV energy band, and of 1.5 mCrab ($\sim 10^{-11}$ erg cm$^{-2}$ s$^{-1}$) in the 40–80 keV energy band. The corresponding upper limit in the 3–10 keV energy band was 5 mCrab ($\sim 7 \times 10^{-11}$ erg cm$^{-2}$ s$^{-1}$), consistent with the *XMM–Newton* findings.

## 3 INFRARED AND OPTICAL OBSERVATIONS

### 3.1 Observatorio Astrofisico Guillermo Haro

Near-infrared observations of the field of the 3FGL J0838.8−2829 source were carried out on 2016 January 14 with the 2.1-m telescope of the Observatorio Astrofisico Guillermo Haro (OAGH) in Cananea, Mexico. The telescope is equipped with the CAnanea Near Infrared CAmera (CANICA), which provides an image scale of 0.32 arcsec pixel$^{-1}$, and covers a field of view of about 4 × 4 arcmin$^2$. CANICA observed with the $H$ filter starting at 08:03:46 UT for an exposure of 60 s, and with the $K$ filter starting at 08:13:56 UT for an exposure of 30 s. The counterparts to the three X-ray sources were detected in both bands, with the following magnitudes: $H = 17.16 \pm 0.2$ and $K = 16.18 \pm 0.09$ for RX J0838−2827; $H = 17.0 \pm 0.2$ and $K = 16.7 \pm 0.1$ for XMM J083850.4−282759; and $H = 17.0 \pm 0.2$ and $K = 16.2 \pm 0.1$ for XMM J083842.7−283832. The zero-points were 20.18 and 21.34 for the $H$ and $K$ filters, respectively (see also Fig. 5). Neither XMM J083850.4−282759 nor XMM J083842.7−283832 have a counterpart in the Two-Micron All-Sky Survey (2MASS) catalogue.[5]

### 3.2 *XMM–Newton* optical monitor

The *XMM–Newton* Optical/UV Monitor Telescope (OM; Mason et al. 2001) was configured in 'Image' mode throughout the first observation and used the $V$ filter, providing a wavelength coverage within the range 5100–5800 Å A total of 10 exposures were acquired, resulting in a total dead-time-corrected on-source exposure time of about 45.8 ks (the first five exposures had a duration of about 5 ks each, whereas the following five lasted about 4.16 ks). The OM acquired the data in both 'fast-window' and 'Image' modes during the second observation, using the $B$ filter (centred on 4392 Å and with band pass between 3800 and 5000 Å). No useful analysis could be carried out on the data sets taken in the fast-window mode, because the source fell outside the small square window (23 × 23 pixel$^2$) of the instrument. We then focused on the data in the 'Image' mode, which consists of fifteen 4.4-ks frames for a total exposure of 66.0 ks.

We extracted the background-subtracted photometric data using the OMICHAIN processing pipeline with the default parameter settings, as recommended by the SAS threads.[6] Only one source was detected within the error circle of the X-ray position of RX J0838−2827, for which we show the light-curve in Fig. 2. The optical emission clearly shows a variability correlated with the X-ray emission, around an average value of 17.77 mag in the $V$ filter and of 17.53 mag in the $B$ filter (expressed in the Vega photometric system). XMM J083850.4−282759 and XMM J083842.7−283832 are clearly detected in the second, longest observation. Interestingly, the former source exhibits a flare ($B \sim 19.5$ mag) simultaneous with that observed in the soft X-ray flux (see Section 6 and Fig. 6). No significant flaring episodes are observed in the data sets of the latter source.

[3] See http://www.swift.ac.uk/analysis/xrt/rmfarf.php
[4] See http://www.swift.ac.uk/analysis/xrt/digest_cal.php
[5] See http://www.ipac.caltech.edu/2mass/releases/second/
[6] See http://xmm2.esac.esa.int/sas/8.0.0/documentation/threads/omi_thread.html.

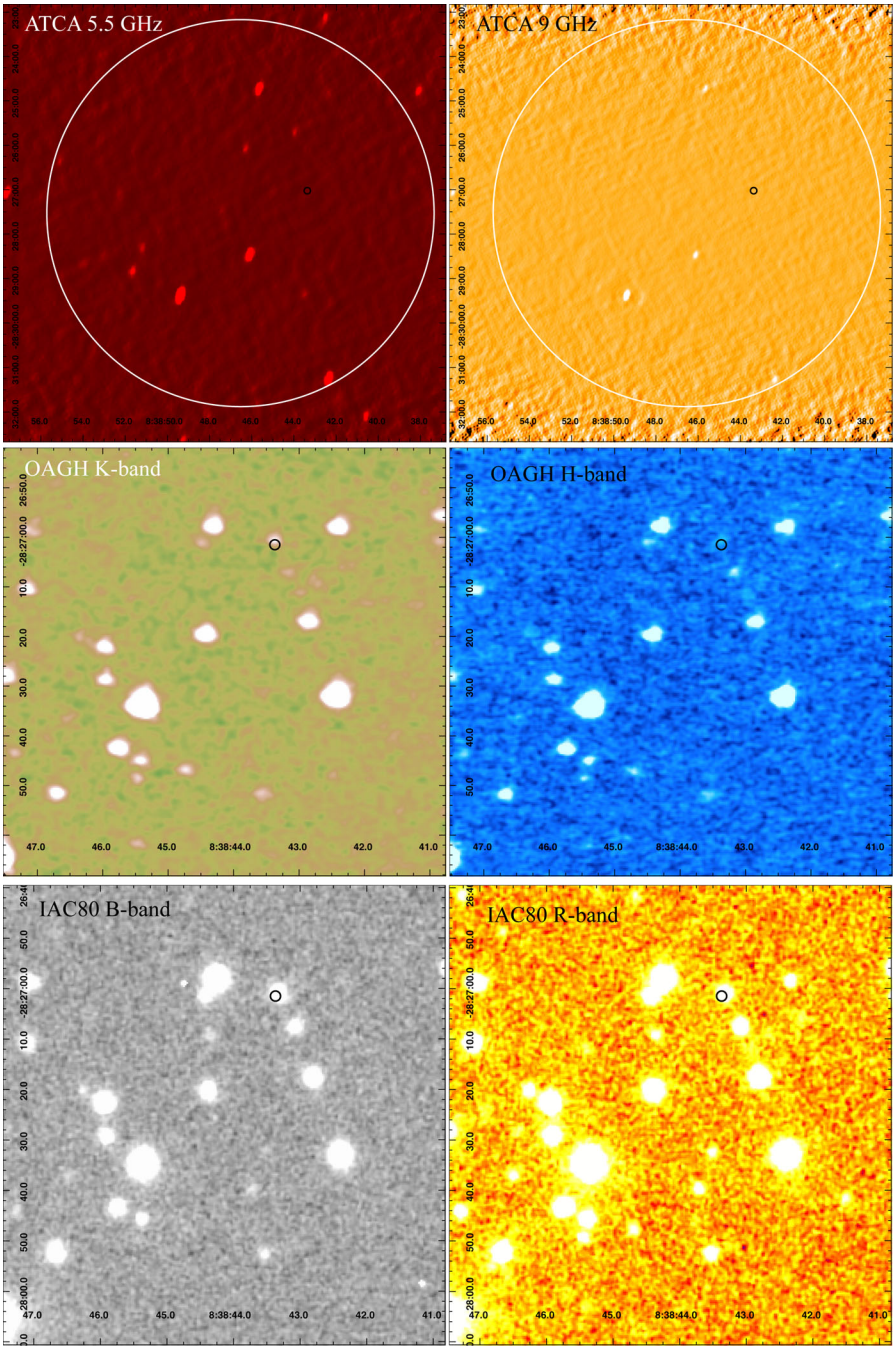


**Figure 5.** Field around RX J0838−2827 in various energy bands. The radio images were taken by ATCA. The top panels show images at 5.5 GHz (top left) and 9 GHz (top right): superimposed are the *Fermi*-LAT 3FGL position (0.°033 error circle at the 68 per cent confidence level), and a 2-arcsec black circle around the optical position of RX J0838−2827. The middle panels show the infrared *K* band (middle left) and *H* band (middle right) as observed by the OAGH telescope. The bottom panels show the optical *B* band (bottom left) and *R* band (bottom right) from the IAC80 telescope. The black circle in the middle and bottom panels is centred on the RX J0838−2827 best optical position with an error radius of 1 arcsec (increasing the optical positional accuracy by a factor of 5 for imaging purposes). North is up, and east is left.

### 3.3 IAC-80

Optical imaging observations of the field of 3FGLJ0838.8-2829 were carried out with the IAC-80 telescope on 2015 December 11 and 12 (MJD 57367 and 57368) and on 2016 January 5 and 28 (MJD 57392 and 57415). A set of exposures lasting 300 s were obtained on each night, alternating the *B* and *R* filters. Image reduction was carried out by following the standard procedures: subtraction of an averaged bias frame, division by a normalized flat frame. Astrometry was performed using the USNOB1.0[7] catalogue. Aperture photometry was carried out with the PHOTOM software part of the STARLINK[8] package. The photometric calibration was performed against the APASS catalogue. In order to minimize any systematic effect, we

[7] http://www.nofs.navy.mil/data/fchpix/
[8] http://starlink.eao.hawaii.edu/starlink

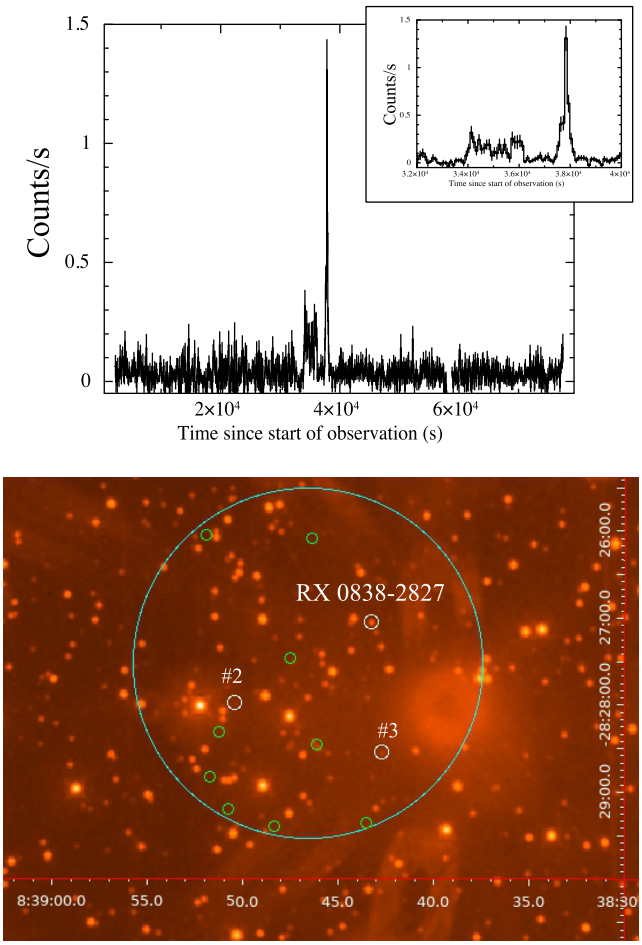


**Figure 6.** *Top*: 0.2–10 keV background-subtracted and exposure-corrected pn light-curve of source no. 2 (XMM J083850.4−282759) during the second *XMM–Newton* observation. A binning time of 400 s was adopted in the inset with the zoom of the flare. Time is in units of seconds since the start of the exposure. *Bottom*: *XMM*-OM field of view with superimposed the 68 per cent *Fermi*-LAT position of 3FGL J0838.8−2829 (light blue) and the three X-ray sources detected in the *XMM*-pn field of view (white). Green denotes the position of all the radio detections at 5.5 GHz within the 3FGL error circle (see text for details).

performed differential photometry with respect to a selection of local isolated and non-saturated standard stars. In Fig. 5 we show two images taken on 2015 December 11 in the *B* and *R* bands. We detected the three X-ray sources in both bands. RX J0838−2827 displays significant variability matching the periodicity observed in the X-ray and with the OM. The mean magnitudes are $B \sim 17.7$ and $R \sim 17.0$. The other two X-ray sources were detected with mean magnitudes $B \sim 21.7$ and $R \sim 19.8$ for XMM J083850.4−282759 and $B \sim 20.0$ and $R \sim 19.01$ for XMM J083842.7−283832. This last source shows a steady optical flux. In contrast, some variability is revealed in XMM J083850.4−282759 both in the single *R*-band exposures (in the *B* band the source is too faint to be detected in the single frames) and among the different nights (Table 3).

### 3.4 ESO-NTT observations

We performed optical spectral observations of RX J0838−2827 on 2016 February 27 with the ESO-NTT telescope (ID: 296.D-5034; PI: Rea). The observations were carried out with the EFOSC2 spectrograph using grism 19 and a slit aperture of 1 arcsec, covering the spectral range 4445–5110 Å with a resolution $R \sim 2500$ (0.67 Å pixel$^{-1}$). A total of 29 spectra, each one lasting 550 s, were obtained in the time interval from 01:05:30 UT to 06:55:33 UT. Data were reduced with standard procedures using the ESO-MIDAS package for bias subtraction and flat-field correction. Wavelength calibration was carried out using helium–argon lamps. The acquired spectra are shown in Figs 7 and 8.

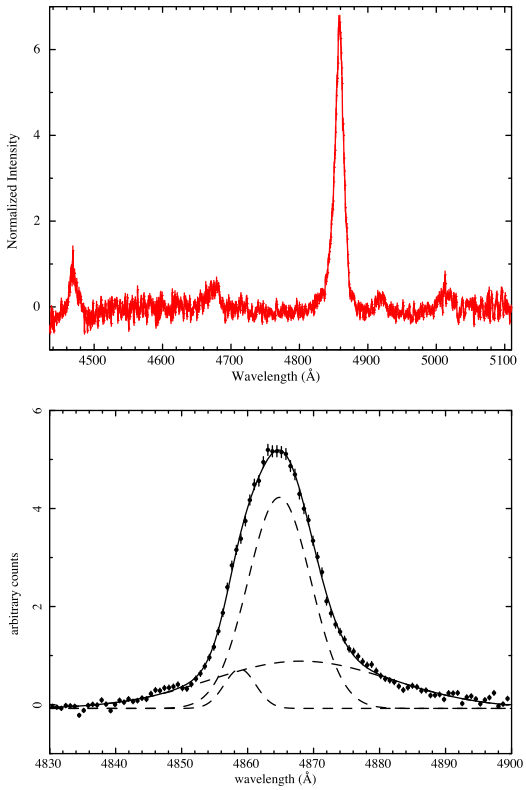


**Figure 7.** *Top*: An example of the ESO-NTT spectra of RX J0838−2827. *Bottom*: Modelling of the H$\beta$ emission line with three Gaussians (see text for details).

## 4 RADIO OBSERVATIONS

We observed the field around the position of 3FGL J0838.8−2829 using the Australia Telescope Compact Array in the 1.5A configuration at 5.5 and 9 GHz with a bandwidth of 2 GHz at each frequency (TOO project CX339). The observations were carried out on 2015 December 4 from 12:46 to 20:28 (UT), with a total integration time of 6.2 h. We used PKS B1934-638 as the flux calibrator and 0858-279 as the phase calibrator. After standard calibration and imaging with MIRIAD (Sault, Teuben & Wright 1995), we ran one round of phase self-calibration and one round of complex amplitude self-calibration. The resulting images (with robust, 0.5 weighting) have an rms of 6.3 and 7.1 μJy at 5.5 and 9 GHz (see Fig. 5). The synthesized beam sizes are 11.1 arcsec by 2.3 arcsec (P.A. −6.5°) and 7.35 arcsec by 1.75 arcsec (P.A. −6.5°), respectively. We detected no radio source at the position of RX J0838−2827 nor at those of the other two X-ray sources down to a 3$\sigma$ upper limit of ∼20 μJy at both frequencies. Other unidentified sources were detected in the field (see Figs 5 and 6).

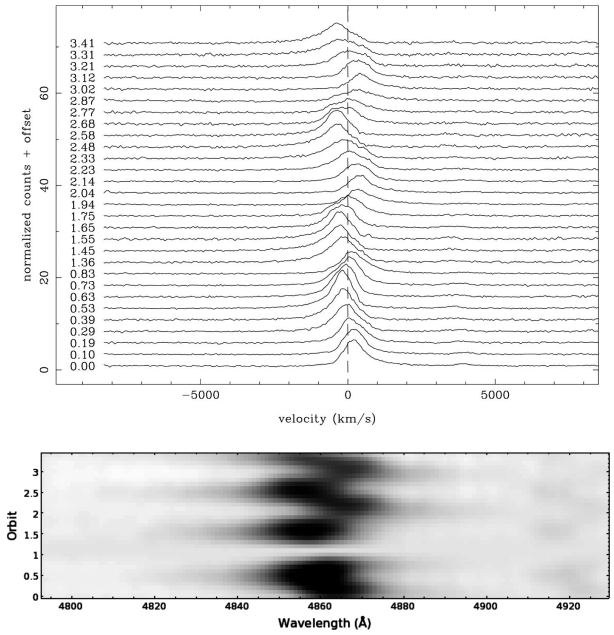


**Figure 8.** ESO-NTT spectra of RX J0838−2827. *Top*: The $H_\beta$ emission line as a function of the orbital phase (computed assuming phase zero for the first NTT spectrum). *Bottom*: Trailed spectra centred on the $H_\beta$ emission line; orbital phases are relative to the 1.64-hr periodicity.

## 5 RX J0838−2827: DATA ANALYSIS AND RESULTS

### 5.1 X-ray timing analysis

The light-curves of the two *XMM–Newton* observations of RX J0838−2827 reveal substantial variations with time (see Figs 2, 9 and 10). A strong modulation with period of ∼1.6 h (6 ks) is easily recognisable, with another ample modulation on a time-scale approximately 10 times longer. Because the longer modulation is present in both the *XMM–Newton* observations, it might be recurrent, with a characteristic time of ∼15 h (54 ks).

The modulation pattern is complex, and we lacked knowledge of its origin, so we adopted the following approach to model it: we

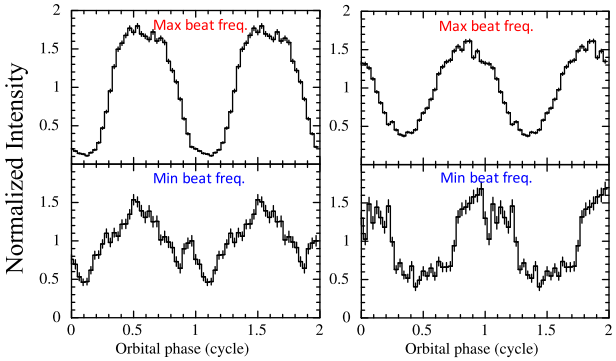


**Figure 10.** *XMM–Newton* light-curves for the first (left) and second (right) observations folded at the system orbital period. The top panels are relative to the time-span of the maximum of the beat modulation, and the bottom panels to the minimum.

first fitted two sinusoidal functions to the data of each observation independently. Because the fit was not satisfactory, we tested the addition of further sinusoidal components with periods free to assume any value (i.e. we did not force them to be integer factors or multiples of $P_1$ or $P_2$). In other words, we modelled the data with a Fourier sum of the form

$$A_0 + \sum_{k\geqslant 2} A_k \sin\left(\frac{2\pi(x-\phi_k)}{P_k}\right). \quad (1)$$

Of course, as $k$ increases, the adherence of the model to the data improves, but we found that the simplest function that fits the data reasonably well, adequately describing the occurrence of minima and maxima and the overall shape of the curve, requires three sine components ($k = 3$). By fitting this purely phenomenological model to the data, we derived the values $P_{1,\mathrm{XMM1}} = 1.644 \pm 0.005$ h (5.92 ± 0.02 ks), $P_{2,\mathrm{XMM1}} = 15.0 \pm 0.5$ h (54.2 ± 2.0 ks), and $P_{3,\mathrm{XMM1}} = 1.491 \pm 0.008$ h (5.37 ± 0.03 ks) for the first *XMM–Newton* observation, and $P_{1,\mathrm{XMM2}} = 1.650 \pm 0.003$ h (5.94 ± 0.01 ks), $P_{2,\mathrm{XMM2}} = 15.2 \pm 0.2$ h (54.7 ± 0.7 ks), and $P_{3,\mathrm{XMM2}} = 1.477 \pm 0.003$ h (5.34 ± 0.01 ks) for the second. The measures of $P_1$ and $P_2$ are not precise enough to bootstrap a unique coherent solution

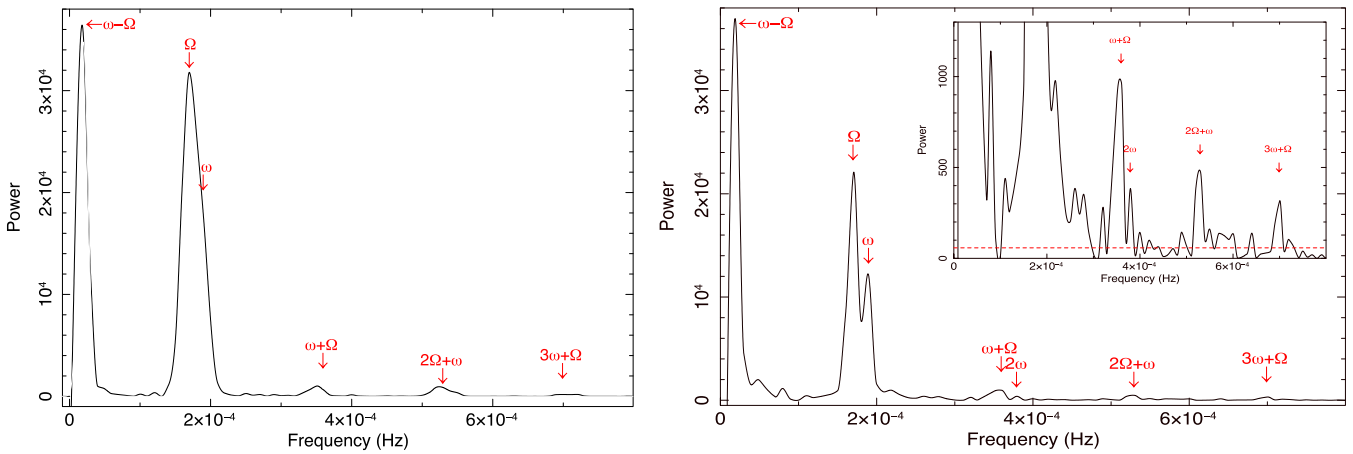


**Figure 9.** Power spectral distribution of RX J0838−2827 computed from the pn data of the first (left) and the second (right) *XMM–Newton* observations. The frequencies/peaks corresponding to the 1.64-h and 1.47-h modulations of the light-curves are identified by Ω and $\omega$, respectively, and several other significant peaks can be interpreted as sidebands or higher harmonics of these frequencies (see Section 5.1). The inset is a zoom of the $y$-axis for purposes of clarity; the dashed line represents the $5\sigma$ significance threshold.

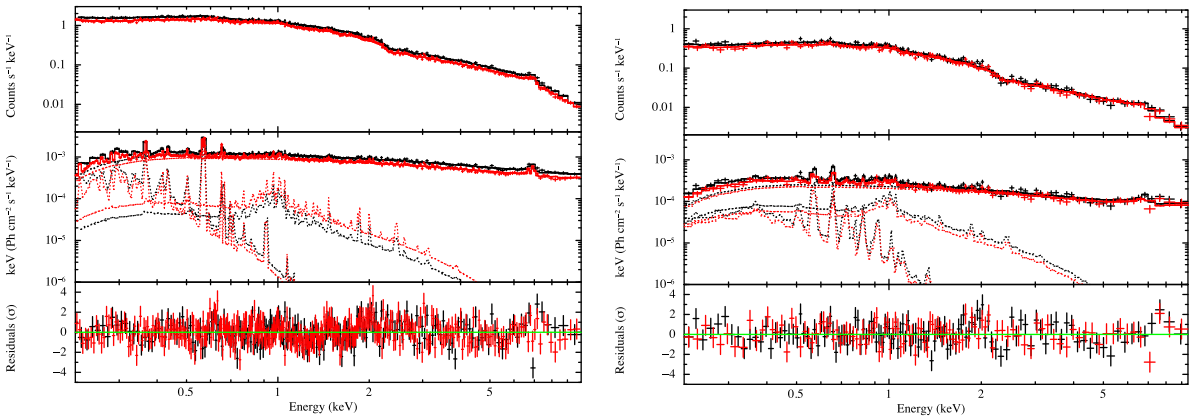


**Figure 11.** The left panel shows the results of the spectral analysis of the peak spectra of the long-term modulation, while the right panel shows the results of the minima. From top to bottom (in both panels): 0.2–10 keV pn spectra of RX J0838−2827 fitted to the TBABS*PCFABS*(MEKAL+MEKAL+MEKAL) model (solid lines); $E \times f(E)$ unfolded spectra; post-fit residuals in units of standard deviations. The first observation is represented in black; the second in red.

that links the two *XMM–Newton* data sets (in particular, there is a strong alias degeneracy in $P_1$).

In order to better assess the situation, we inspected a Fourier transform of the second *XMM–Newton* observation computed using the pn data that allow the highest timing resolution (bin time: 47.66 ms). Several peaks can be observed in the power spectral density (PSD) plot (Fig. 9). Two strong close but distinct peaks (their separation is larger than the intrinsic Fourier resolution, $\Delta\nu \simeq 1.4 \times 10^{-5}$ Hz) are located at $\Omega = 1.69(5) \times 10^{-4}$ Hz (the central frequency was measured by the fit with a Gaussian, and is equivalent to $1.64 \pm 0.04$ h) and $\omega = 1.88(9) \times 10^{-4}$ Hz ($1.47 \pm 0.08$ h), and they clearly correspond to $P_{1,\mathrm{XMM2}}$ and $P_{3,\mathrm{XMM2}}$, respectively. An even higher peak is present at $\sim 1.87 \times 10^{-5}$ Hz (14.88 h) and is consistent with $P_{2,\mathrm{XMM2}}$. The fact that the central frequency of this peak differs by less than 2 per cent from the quantity $\omega$–$\Omega$ strongly suggests that the peak is the sideband (beat) frequency between $\Omega$ and $\omega$, which we interpret as the orbital and spin periods of RX J0838−2827, respectively (see Section 7.1). Many other peaks that stand out above the significance threshold in the PSD can be interpreted as combinations of $\Omega$ and $\omega$. The most prominent ones are labelled in Fig. 9. The PSD computed from the first observation is similar (Fig. 9), but only one peak is present around the frequencies of $\Omega$ and $\omega$. This is to be expected in any case, because of the lower intrinsic resolution of this observation ($\sim 2.2 \times 10^{-5}$ Hz), but the slightly asymmetric shape of the peak, which is unbalanced towards $\Omega$, suggests that it may actually be a blend of two peaks.

### 5.2 X-ray spectral analysis

We started the spectral analysis by fitting the pn averaged spectra of the two observations to a set of models: power laws, bremsstrahlung, blackbodies, an accretion disc consisting of multiple blackbody components (DISKPBB), a model describing the emission produced by a thermal distribution of electrons that Compton up-scatter soft seed X-ray photons (NTHCOMP; Zdziarski, Johnson & Magdziarz 1996; Życki, Done & Smith 1999), and a model reproducing the emission by hot diffuse gas (MEKAL). We accounted for photoelectric absorption by the interstellar medium along the line of sight through the TBABS model, and adopted the photoionization cross-sections from Verner et al. (1996) and the chemical abundances from Wilms, Allen & McCray (2000). None of the above-mentioned models gave a satisfactory description of the data.

Much more acceptable results were achieved when fitting the data to models consisting of several MEKAL components at different temperatures.

Given the strong flux variability in both observations, as well as the variable hardness ratio we observed comparing light-curves in different energy bands (see Fig. 2), we performed the spectral analysis comparing time-resolved spectra, which we believe yielded more meaningful results for this variable source (see Fig. 11). We first analysed the spectra during the peak of the 54.7-ks beat modulation for both observations, and then we extracted spectra for the maximum and minimum of the shorter 5.9-ks periodicity. When fitting with a series of 3MEKAL models we found good results for all the spectra we considered. Despite the cycle-to-cycle variations observed in the hardness ratio in both observations (see Fig. 2), we did not find significant variability (within the 90 per cent parameter uncertainties) when fitting the 1.64-h phase-dependant spectra nor merging the two observations in phase to increase the statistics of each phase-resolved spectrum (probably owing to the low number of counts that we could collect at the minimum phases). However, we found significant changes in the spectra collected at the maximum and minimum of the long-term beat period of 54.7 ks. The best-fitting parameters for the absorbed 3 MEKAL model are listed in Table 2, and the spectrum and the best-fitting model are shown in Fig. 11. It is evident how the relative significance of the three different hot plasmas changes along the beat modulation, with the coolest component at an effective temperature of $\sim$0.2 keV being more prominent at the maxima of the beat ($\omega$–$\Omega$) modulation. This might be because accretion switches to the other (lower) pole at the half-beat cycle, and the other pole might not be visible anymore (depending on the colatitude and the inclination angles).

The source 0.2–10 keV observed flux was $7.6 \times 10^{-12}$ erg cm$^{-2}$ s$^{-1}$, a factor of $\sim$1.2 larger than that measured during the second observation, about 1.5 months later. The derived absorption column density, $N_{\mathrm{H}} \sim 1.6 \times 10^{20}$ cm$^{-2}$, is about one order of magnitude lower than the estimated total Galactic value in the direction of the source ($\sim 2 \times 10^{21}$ cm$^{-2}$; Willingale et al. 2013), implying a close-by location of this source within our Galaxy.

### 5.3 High-resolution X-ray spectra

We used the first-order RGS spectra of both observations to search for narrow features. Two prominent narrow emission lines are clearly detected in both observations, and a few weaker lines were

**Table 2.** Results of the fits of the *XMM–Newton* EPIC pn spectra of RX J0838−2827 at the minimum and maximum of the ∼54.7-ks beat modulation. For each beat phase the spectra of both observations were fitted together to the TBABS*PCFABS*(MEKAL+MEKAL+MEKAL) model, with all normalizations free to vary. Uncertainties are quoted at the 90 per cent confidence level for a single parameter of interest.

| Parameter | Minimum | Maximum |
|---|---|---|
| $N_{\rm H}$[a] ($10^{20}$ cm$^{-2}$) | $2.3^{+0.8}_{-0.6}$ | $2.4 \pm 0.5$ |
| PCFABS $N_{\rm H}$ ($10^{24}$ cm$^{-2}$) | $1.8^{+1.3}_{-0.7}$ | $2.9^{+1.8}_{-1.1}$ |
| Covering fraction ( per cent) | $72^{+18}_{-24}$ | $67^{+23}_{-30}$ |
| $A_Z$ ($A_{Z,\odot}$) | $0.2^{+0.2}_{-0.1}$ | $0.37 \pm 0.1$ |
| $kT_1$ (keV) | $0.22 \pm 0.03$ | $0.12 \pm 0.02$ |
| Normalization[b] | $7.1^{+1.8}_{-0.3}$ (obs 1) | $30.2^{+6.7}_{-1.8}$ (obs 1) |
| | $5.2^{+1.4}_{-0.3}$ (obs 2) | $21.3^{+4.7}_{-1.3}$ (obs 2) |
| $kT_2$ (keV) | $1.03 \pm 0.14$ | $1.00 \pm 0.08$ |
| Normalization | $8.9^{+2.4}_{-0.6}$ (obs 1) | $4.2^{+1.7}_{-0.4}$ (obs 1) |
| | $6.5^{+1.9}_{-0.5}$ (obs 2) | $7.6^{+0.6}_{-0.3}$ (obs 2) |
| $kT_3$ (keV) | $11.7^{+7.3}_{-2.6}$ | $14.8^{+1.2}_{-0.9}$ |
| Normalization | $38^{+7.7}_{-1.7}$ (obs 1) | $161^{+31}_{-8}$ (obs 1) |
| | $34^{+6.9}_{-1.6}$ (obs 2) | $130^{+13}_{-6}$ (obs 2) |
| Absorbed flux[c] | $2.3 \pm 0.7$ (obs 1) | $10.3 \pm 1.0$ (obs 1) |
| | $2.0 \pm 0.7$ (obs 2) | $8.4 \pm 1.2$ (obs 2) |
| $\chi^2_\nu$ (dof) | 1.09 (213) | 1.06 (541) |
| Null hypothesis probability | $1.5 \times 10^{-1}$ | $1.3 \times 10^{-1}$ |

*Notes*. [a]The abundances are those of Wilms, Allen & McCray (2000). The photoelectric absorption cross-sections are from Verner et al. (1996).
[b]Normalizations are in units of $10^{-4}$ cm$^{-5}$.
[c]Fluxes are in units of $10^{-12}$ erg cm$^{-2}$ s$^{-1}$ and in the 0.2–10 keV energy range.

**Table 3.** Log of IAC80 imaging observations and results of photometry of the source XMM J083850.4−282759. Magnitudes are in the Vega system and are not corrected for Galactic extinction.

| Mid exp. time (MJD) | Exposure time (s) | Filter | Mag |
|---|---|---|---|
| | XMM *J*083850.4 − 282759 | | |
| 57367.21949 | 18 × 300s | *B* | $22.20 \pm 0.17$ |
| 57367.22329 | 18 × 300s | *R* | $19.83 \pm 0.12$ |
| 57368.20316 | 16 × 300s | *B* | $21.86 \pm 0.13$ |
| 57368.20314 | 16 × 300s | *R* | $19.71 \pm 0.12$ |
| 57392.11902 | 11 × 300s | *B* | $21.31 \pm 0.11$ |
| 57392.12283 | 12 × 300s | *R* | $19.55 \pm 0.12$ |
| 57415.07043 | 15 × 300s | *B* | >21.5 (3$\sigma$ U.L.) |
| 57415.06659 | 16 × 300s | *R* | $20.08 \pm 0.15$ |

also significantly detected. All the observed lines were well fitted by the multiple hot ionized plasma models (MEKAL) used to fit the EPIC-pn spectra (see Section 5.2). In particular, in the RGS spectrum of the second *XMM* observations we identified the lines corresponding to: Mg XII H-like Lyman $\alpha$ at 8.42 Å, Ne X H-like Lyman $\alpha$ at 12.13 Å, Ne IX He-like w-resonance at 13.45 Å, O VIII H-like Lyman $\alpha$ (18.97 Å) and $\beta$ (16.01 Å), and a triplet of He-like O VII centred at 21.60 Å (see Fig. 3).

In order to test possible signs of variability among the most prominent lines between the maximum and minimum of the 1.64-h X-ray modulation, we fitted the two phase-resolved RGS data sets (merging data of both observations) with an absorbed power-law plus two Gaussian functions with energies fixed at 21.60 Å (0.57 keV) and 18.97 Å (0.65 keV), and with all spectral parameters forced to be the same except for the normalizations. The equivalent width of the O VII line is $64^{+34}_{-17}$ eV in the RGS spectrum at the maximum of the modulation, while only an upper limit of <62 eV (at 90 per cent) could be derived in the RGS spectrum at the minimum of the 1.64-h modulation. Similarly, the equivalent width of the O VIII line is $33^{+6}_{-13}$ eV in the RGS spectrum at the maximum, and we derived an upper limit of <69 eV at the minimum. No significant phase-dependent variability was detected in the emission lines, and the oxygen lines are well reproduced by the lowest-temperature (∼0.2keV) MEKAL component.

### 5.4 Long-term X-ray light-curve

The long-term light-curve of RX J0838−2827 presented in Fig. 4 was extracted after fitting all *Swift*/XRT spectra with an absorbed power-law model, with the absorption column density fixed to the value derived from the fits of the *XMM–Newton* data (the lower counting statistics of the XRT data precluded a more detailed modelling as carried out for the EPIC data sets). We obtained $\chi^2_\nu = 1.13$ for 203 degrees of freedom. We believe that the large scatter in the flux values clearly visible in the figure (especially in the most recent observations) is probably because the short exposures of the observations (see Table 1) have sampled the source ∼54-ks cycle at random phases. However, the long-term light-curve indicates that no substantial variation has been observed in the source X-ray flux for the last 6 yr.

### 5.5 Results from optical observations

The optical spectra of RX J0838−2827 (see Fig. 7) are dominated by prominent emission lines such as H$\beta$, He I (λ 4471, 4919, 5015), He II (λλ 4686) and possibly Bowen-blend N III (λ 4634–41)/C III (λ 4647–50). No significant absorption feature is detected, in agreement with the findings of Masetti et al. (2013).

Among the emission features detected, H$\beta$ is the most prominent. In the individual spectra we found no evidence for a double-horned profile (usually interpreted as a signature for an accretion disc). The line profile is, however, clearly asymmetric. We tried to model the H$\beta$ line with a set of multiple Gaussians and found a reasonable solution using three Gaussians plus a constant: in Fig. 12 we show the velocities of these three components. The H$\beta$ line consists of a narrow (FWHM=11 Å ∼ 680 km s$^{-1}$), a broad (FWHM ∼ 30 Å ∼ 1900 km s$^{-1}$) and a very narrow (FWHM ∼ 6 Å ∼ 370 km s$^{-1}$) component, the latter statistically detected in only a few spectra (see Fig. 12). The large width of the broad component indicates that it is probably formed in the magnetically confined accretion flow, with the narrow one probably forming in the ballistic trajectory of the accretion stream, and the very narrow one in the irradiated hemisphere of the donor star. These components are generally observed in polars, and particularly in asynchronous polars (see e.g. Schwarz et al. 2005).

Fits to the radial velocity measurements for each line were first attempted using a constant and a sinusoidal function (see Fig. 12). We here use the radial velocities as derived for the H$\beta$ narrow and broad components, and the radial velocity measurements of the other emission lines obtained through a single Gaussian. A fit with a constant plus a single sinusoidal function never provided a satisfactory result in terms of reduced $\chi^2$. We then tried a different approach and fitted each radial velocity curve with the function of equation (1) with $k = 3$, $P_2 = P_{2,\rm XMM2} = 15.2$ h and

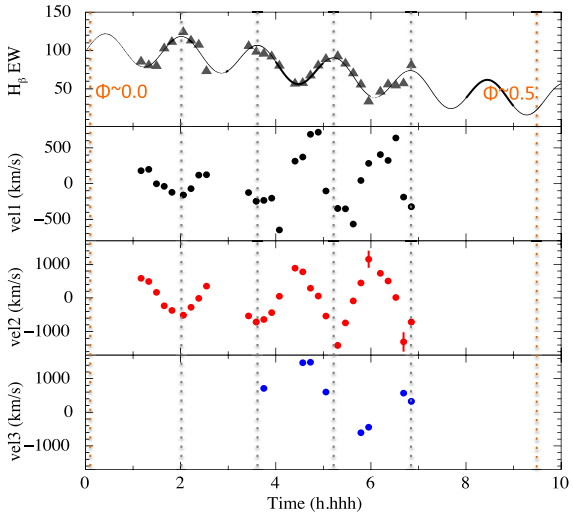


**Figure 12.** Equivalent width of the H$\beta$ line (top panel), and velocities of three H$\beta$ components as a function of time as observed from ESO-NTT. Vertical dashed lines represent the phases 0 and 0.5 of the 15.2-h modulation (orange), and the maxima of the 1.64-h orbital modulation (grey).

$P_3 = P_{3,\rm XMM2} = 1.47$ h (fixed) (see Fig. 12). We measured the following $P_1$ periods: $1.75 \pm 0.05$ h (H$\beta$, first velocity, $\chi^2_\nu$/dof $= 1.40/21$), $1.72 \pm 0.05$ h (H$\beta$, second component, $\chi^2_\nu$/dof $= 0.71/21$), $1.53 \pm 0.01$ h (He I 4480 Å, $\chi^2_\nu$/dof $= 0.67/20$), $1.48 \pm 0.01$ ks (He I 4920 Å, $\chi^2_\nu$/dof $= 4.53/20$), and $1.66 \pm 0.04$ h (He I 5020 Å, $\chi^2_\nu$/dof $= 0.61/20$). From the first H$\beta$ component, we were able to derive some constraints on the amplitudes: $A_0 = -(4 \pm 1) \times 10^2$ km s$^{-1}$, $A_1 = (4.2 \pm 0.5) \times 10^2$ km s$^{-1}$, $A_2 = (6.3 \pm 1.6) \times 10^2$ km s$^{-1}$, $A_3 = (1.7 \pm 0.3) \times 10^2$ km s$^{-1}$. This multi-sinusoidal representation indicates that, in addition to the orbital modulation (with an amplitude of about 400 km s$^{-1}$, see Fig. 8), a fast-moving high-velocity component shifting from a maximum of about +1100 to −1200 km s$^{-1}$ may be caused by the ballistic accretion stream, which also changes along the beat cycle.

For each spectrum, we also measured the equivalent width (EW) of the H$\beta$ and He I emission lines. We found evidence for significant EW variability, as also observed for the optical flux measured by our IAC-80 and *XMM–Newton*/OM observations (see e.g. Fig. 2, right panel, bottom). The EW of all emission features seems to be modulated over the 1.64-h and 15.2-h periodicities, the orbital period and the long-term beat periodicity (see Fig. 12). Because the spectral line EW is a proxy of the source optical flux, such findings are not unexpected.

The NTT data consist of short exposures of ∼500 s each, spanning only a few cycles of the orbital modulation at 1.64 h, for a total observation time of ∼6 h (see Figs 8 and 12). For this reason, when fitting theses data with the multicomponent models used in Section 5.1, we held $P_2$ and $P_3$ at the *XMM–Newton* values measured during the second observation.

Because of the very sparse sampling, long data gaps and short exposures, the IAC80 photometric data are of limited help in constraining the model and/or refining the periods. So, we fixed $P_1 = P_{1,\rm XMM2} = 1.64$ h and $P_3 = P_{3,\rm XMM2} = 1.47$ h (the three-sine model also provides a much better fit for the IAC80 data than the two-sine model). In this way, for the long modulation we found $P_{2,\rm B} \simeq 15.1$ h from the *B*-filter data and $P_{2,\rm R} \simeq 15.2$ h from the *R*-filter data.

## 6 THE TWO OTHER X-RAY SOURCES IN THE FIELD: XMM J083850.4−282759 AND XMM J083842.7−283832

Of the two additional X-ray sources within the field of the mCV, XMM J083850.4−282759 can be identified in the USNO A2 Catalogue at RA $= 08^{\rm h}38^{\rm m}50\overset{\rm s}{.}4$, Dec.$= -28^\circ27'56\overset{''}{.}7$ (J2000.0) with $R = 18.0$ and $B = 20.6$, and XMM J083842.7−283832 is catalogued in the Wide-field Infrared Survey Explorer (WISE;[9] Wright et al. 2010) as WISE J083842.77−282830.9. Its position is RA $= 08^{\rm h}38^{\rm m}42\overset{\rm s}{.}777$, Dec. $= -28^\circ28'30\overset{''}{.}99$ (J2000.0), and it has optical magnitudes in the USNO B1 Catalogue of $B1 \sim 19.66$, $B2 \sim 18.49$, $R2 \sim 19.02$ and $I \sim 18.01$.

We carried out a detailed X-ray spectral and timing analysis for both sources. XMM J083850.4−282759 appears to be variable in the X-ray (see the values for the root mean square fractional variation and fluxes in Table 4), and showed a flare lasting for ∼600 s with a structured morphology in the second observation (see Fig. 6).[10] For both sources, spectra of the two observations were fitted together with an absorbed power-law model, and the absorption column density was tied up across the data sets (for the case of XMM J083850.4−282759 both the flare and quiescent spectra were extracted). The best-fitting parameters are reported in Table 4. The steady emission of XMM J083850.4−282759 is brighter during the second observation by a factor of ∼5, while showing the flaring episode, and its spectrum is slightly harder than in the first observations. In contrast, XMM J083842.7−283832 appears to be steady during the X-ray observations.

## 7 DISCUSSION

Our multiband study of the field of 3FGL J0838.8−2829 revealed two variable X-ray sources: RX J0838−2827 and XMM J083850.4−282759. Here we discuss our results and the nature of these two intriguing objects.

### 7.1 RX J0838−2827: an asynchronous magnetic CV

RX J0838−2827 has been shown to be highly variable on short and long time-scales with a complex behaviour. In particular, we detect two dominant periodicities, at 1.64 h and 15.2 h in the power spectrum, as well as a 1.47-h peak, which has about half the power of the 1.64 h one (see Fig. 9). These are remarkably well correlated, as the long periodicity is found at precisely the beat between the two shorter ones. These characteristics and their time-scales are uncommon in other variable X-ray sources, such as the LMXBs, but are consistent with those observed in CVs of the magnetic type. The close 1.64-h and 1.47-h periods, if interpreted as the binary orbital period and the rotational period of the WD, give $P_{\rm spin}/P_{\rm orb} \sim 0.90$. The location of RX J0838−2827 in the spin–orbit period plane of mCVs is shown in Fig. 13, and strongly suggests that this system is close to, but not right at, synchronism. We therefore have identified either one of the slowest-rotating IPs (see also Coti Zelati et al. 2016) or a highly de-synchronized polar. Other weakly asynchronous magnetic systems with similar spin–orbit ratios are Paloma with $P_{\rm spin}/P_{\rm orb} \sim 0.93$ (Schwarz et al. 2007), and IGR J19552+0044 with $P_{\rm spin}/P_{\rm orb} \sim 0.82$ (Bernardini et al. 2013). The other four confirmed asynchronous polars

[9] See http://wise2.ipac.caltech.edu/docs/release/allsky/

[10] A careful analysis of the background light-curve excludes a background flare origin.

**Table 4.** Positions, pn count rates and spectral fit results for the X-ray sources within the error box of 3FGL J0838.8−2829. The source numbering is as shown in Fig. 6. The pn spectra were fitted to the TBABS*PEGPWRLW model in the energy range 0.2–10 keV. Uncertainties are quoted at a 90 per cent confidence level for a single parameter of interest, whereas upper limits are given at the $3\sigma$ confidence level. (q) and (f) refer to the quiescent and flaring states of XMM J083850.4−282759, respectively, during the second observation.

| Source | Obs ID | RA (J2000.0) | Dec. | Count rate[a] ($\times 10^{-3}$ s$^{-1}$) | rms[b] | $N_{\rm H}$ ($10^{21}$ cm$^{-2}$) | $\Gamma$ | Unabs. flux[a] ($10^{-14}$ erg cm$^{-2}$ s$^{-1}$) | $\chi^2_\nu$ (dof) |
|---|---|---|---|---|---|---|---|---|---|
| XMM J083850.4−282759 | 0764420101 | $08^h38^m50\overset{s}{.}40$ | $-28°27'59\overset{''}{.}04$ | 16.7 ± 0.9 | 0.37 ± 0.06 | 0.3 ± 0.2 | 1.6 ± 0.2 | 8 ± 1 | 0.97 (63) |
| | 0790180101 | | | 74 ± 2 (q) | 1.23 ± 0.07 | tied | 1.15 ± 0.08 (q) | 38 ± 3 (q) | |
| | | | | 1223 ± 82 (f) | | tied | 1.3 ± 0.2 (f) | 550 ± 90 (f) | |
| XMM J083842.7−283832 | 0764420101 | $08^h38^m42\overset{s}{.}72$ | $-28°28'32\overset{''}{.}52$ | 22.1 ± 0.9 | <0.18 | 1.1 ± 0.3 | 1.9 ± 0.2 | 11.1 ± 0.9 | 0.94 (27) |
| | 0790180101 | | | 14.8 ± 0.8 | <0.17 | tied | 2.1 ± 0.2 | 8.6 ± 0.9 | |

*Notes*. [a]In the 0.2–10 keV energy range.
[b]Root mean square fractional variation, determined by applying the LCSTATS (v. 1.0) tool of XRONOS on the 0.2–10 keV background-subtracted and exposure-corrected light-curves from the pn camera with a binning time of 400 s.

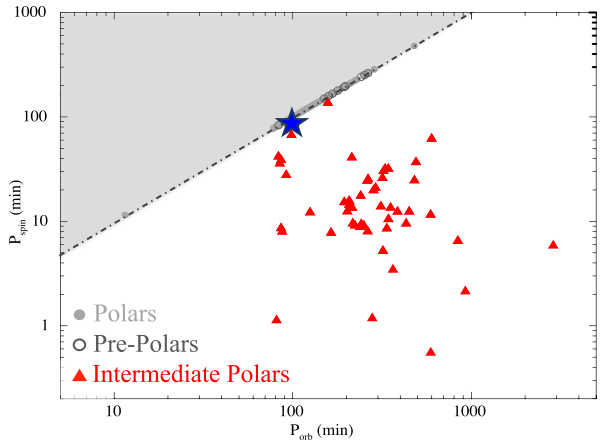


**Figure 13.** Orbital and spin periods of polars (grey dots), pre-polars (dark grey circles), and IPs (red triangles) known to date, with the values derived for RX J0838−2827 shown as a blue star. The dot–dashed line represents $P_{\rm spin} = P_{\rm orb}$. Data adapted from Ferrario, de Martino & Gänsicke (2015).

**Table 5.** Main properties of the slightly desynchronized mCVs currently known (in order of increasing degree of asynchronism).

| System | $P_{\rm spin}$ (s) | $P_{\rm orb}$ (s) | $P_{\rm spin}/P_{\rm orb}$ | $P_{\rm beat}$ (h) |
|---|---|---|---|---|
| V 1432 Aquilae | 12 150 | 12 116 | 1.002 | 1 213.4 |
| CD Ind | 6 579 | 6 649 | 0.989 | 175.2 |
| BY Camelopardalis | 11 961 | 12 089 | 0.989 | 348.5 |
| RX J0838−2827 | 5 340 | 5 940 | 0.898 | 15.2 |
| Paloma | 7 800 | 9 360 | 0.833 | 13.0 |
| IGR J19552+0044 | 4 960 | 6 100 | 0.813 | 7.3 |
| EX Hydrae | 4 022 | 5 895 | 0.682 | 3.5 |

*Notes*. *The listed values are taken from: V 1432 Aquilae, Mukai et al. (2003); CD Ind, Myers et al. (2017); BY Camelopardalis, Silber et al. (1997); RX J0838−2827, this study; Paloma, Joshi et al. (2016); IGR J19552+0044, Bernardini et al. (2013); EX Hydrae, Mauche et al. (2009).

are only very slightly de-synchronized ($P_{\rm spin}/P_{\rm orb} > 0.98$; see also Fig. 5).

Folding the X-ray light-curve at the 1.64-h period (see Fig. 10; or at the 1.47-h period) the shape is almost flat-topped, closely resembling the shapes observed in strongly magnetic polar systems (Cropper 1990), where the modulation is caused by the self-occultation of the accretion pole as the WD rotates. The spectrum is thermal, requiring three optically thin emitting regions with temperatures of 0.2, 1 and 14 keV, highly absorbed by dense partial (∼70 per cent) covering material ($\sim 2 \times 10^{24}$ cm$^{-2}$). The spectral characteristics also closely resemble those observed in magnetic CVs, both polars and IPs (e.g. Ramsay & Cropper 2004; Bernardini et al. 2012). The lack of spectral changes (except for the normalization) at the ∼1.6–1.5 h periods is consistent with the spectral behaviour seen in polars owing to the self-occultation of the main accreting pole, while IPs instead show highly variable absorption along the spin period. Furthermore, and in contrast to many polars, RX J0838−2827 does not show any evidence of a soft optically thick (blackbody) component. This component originates from the reprocessing of hard X-rays and cyclotron radiation in the WD polar regions. The presence of this component was for a long time considered ubiquitous in polars, until recent observations showed that this is not necessarily so (Ramsay & Cropper 2004). On the other hand, IPs have typically hard spectra, and the recent identification of a soft blackbody component in about 30 per cent of these systems (Anzolin et al. 2008; Bernardini et al. 2012) does not make these characteristics an identifying feature of one or the other type of mCVs.

The long observations acquired with *XMM–Newton* have allowed an unprecedented monitoring of RX J0838−2827, revealing a remarkable long-term 15.2-h X-ray modulation that repeats itself in the two observations taken 1.5 months apart, which we naturally interpret as the beat period between the 1.64- and 1.47-h periodicities. The spectrum changes mainly in the normalizations of the optically thin components and in the temperature of the warmer plasma, but not in the partial absorption components. This further strengthens our interpretation that this variability is not the orbital period because the orbital X-ray variability in the asynchronously rotating IPs is found to be caused by absorbing material fixed in the binary frame, such as the hotspot at the rim of an accretion disc or eclipses in high-inclination systems (see Parker, Norton & Mukai 2005). The optical radial velocities of emission lines and the optical light also give evidence for the presence of such long variability, implying that it does not arise from X-ray irradiation on an accretion disc as seen in many IPs (see Warner 2003). The presence of this modulation in both the X-ray and optical implies a disc-less configuration (Wynn & King 1992), in which the accreting material alternates onto the WD poles. In non-synchronous systems, the flow rotates around the magnetic field of the WD on a time-scale of the beat period. This has the effect that the flow will be preferentially directed onto the first (main) pole and then onto the other, each

half-beat cycle. The weaker modulations at the 1.47- and 1.64-h periods at about half the 15.2-h beat period indicate that there is pole-switching in RX J0838−2827.

In particular, disc-less models predict the dominance of the beat and of the orbital frequencies and a much lower or even undetectable spin peak in the power spectrum in configurations of moderately high values of the binary inclination angle ($i$) and magnetic colatitude ($m$), provided that $i + m > 90^o + \beta$, where $\beta$ is the pole-cap opening angle (Wynn & King 1992). The presence of lower peaks at sidebands depends on the pole-switching effect that modulates the light-curve. Furthermore, the power of the spin peak is dependent on the degree of asymmetry, with strong asymmetries producing weaker spin pulsations (Wynn & King 1992). This appears to be the case in RX J0838−2827. In addition, the slope of the beat modulation depends on the transition times of accretion flipping onto the two poles, and thus the almost smooth variability at the 15.2-h period would indeed indicate that the stream from the donor star does not switch between the two poles instantaneously. We further note that a large $\beta$ tends to produce either sinusoidal or flat-topped light curves, indicating that accretion in RX J0838−2827 occurs over wide areas of the WD poles. Furthermore, the faint phase of the modulation at the 1.64-h (or 1.47-h) period (see Fig. 10) observed at beat maximum lasts ∼0.3. This can be used to estimate the ranges of binary inclination $i$ and magnetic colatitude $m$ (Cropper 1990), as $\cot\, i = \cos(\pi\, \delta\phi)\, \tan(m)$, where $\delta\phi$ is the length of the faint phase. Moreover, the lack of X-ray eclipses restricts $i \lesssim 75^\circ$. We then find $24^\circ \lesssim m \lesssim 59^\circ$ for $10^\circ \lesssim i \lesssim 75^\circ$. A detailed modelling of accretion regions is, however, beyond the scope of this work and will be the subject of a future publication. Flipping accretion configurations are probably also occurring in other asynchronous systems such as Paloma (Schwarz et al. 2007), BY Cam (Piirola et al. 1994), CD Ind (Ramsay et al. 1999) and V1432 Aql (Mukai et al. 2003). In the latter system, the hard X-ray emission is found to be dominated by the orbital variability along the beat cycle, while the X-ray spin variability is almost undetected in a long *BeppoSAX* observation (Mukai et al. 2003) and with complex structure in *XMM–Newton* and *RXTE* observations (Rana et al. 2005).

The short orbital period of RX J0838−2827 puts this mCV below the 2–3-h orbital period gap of CVs, where most polars are found (Ferrario et al. 2015; see also Fig. 13). An orbital period of 1.64 h (98 min) is close to that of the IP EX Hya, which is also (but not so weakly) de-synchronized ($P_{\rm spin} \sim 67$ min). Its spin–orbit period ratio ($P_{\rm spin}/P_{\rm orb} = 0.68$), similar to that of the few IPs found below the gap, could indicate that these systems will never reach synchronism (see Norton et al. 2004). Regarding the other two weakly de-synchronized mCVs, Paloma and IGR J19552+0044, they are both short-period systems. The former, with a 157-min orbital period, falls inside the orbital period gap, and the second, with a 101-min orbital period, is below the gap. They are probably in a transition stage before reaching synchronism, and are thus believed to be polar progenitor candidates. On the other hand, the four asynchronous polars are less de-synchronised. Synchronization time-scales of ∼170 and ∼200 yr were found in V1500 Cyg (Harrison & Campbell 2016) and V1432 Aql (Staubert et al. 2003), respectively, suggesting that the cause was probably a nova explosion in the past. The lack of nova shells around the four systems is not, however, evidence against the nova interpretation, because many old novae do not show such relics (Pagnotta & Zurek 2016).

Therefore, given the closer similarities of spin–orbit period ratios to Paloma and IGR J19552+0044, rather than to the four asynchronous polars, we suggest that RX J0838−2827 is in a similar evolutionary stage. A spectro-polarimetric study will provide tight constraints on the magnetic field and geometry of this new interesting mCV and its evolution.

### 7.2 XMM J083850.4−282759: a candidate transitional millisecond pulsar?

The identification of RX J0838−2827 as an asynchronous polar argues against its identification as a possible counterpart of the *Fermi*-LAT gamma-ray source 3FGL J0838.8−2829, because emission at ∼GeV energies has to date never been reported from CVs. One possibility might be that the gamma-ray emission is associated with one of the two faint X-ray sources detected in the *Fermi*-LAT error circle.

As reported in Table 4, the absorption column density derived from the X-ray spectrum of XMM J083850.4−282759 is $N_{\rm H} \sim 3 \times 10^{20}$ cm$^{-2}$, about one order of magnitude lower than the total Galactic value in the direction of the source. Assuming that the full observed column density contributes to the optical/near-infrared absorption, we estimate a colour excess $E(B-V) = 0.05$ mag (using the $N_{\rm H}/E(B-V)$ conversion of Predehl & Schmitt 1995). From the results of our optical and near-infrared photometry (Sections 3.1 and 3.3), we obtain for this source a de-reddened $B-R$ colour in the range 1.5–2.5 mag (taking into account the source variability and the uncertainties in the photometry) and $H-K = 0.3 \pm 0.2$ mag, broadly consistent with a late-type K2–M5 main sequence star. Under this hypothesis, using the distance modulus, the constraints on the source distance are very broad, ranging from 0.7 (M5) to 6.2 (K2) kpc.

In light of the observed colours, a coronal flare from an M-type star could be an explanation for the brightening observed in the *XMM–Newton* X-ray and optical light curves shown in Fig. 6. However, considering the inferred distance, the average X-ray flux (∼$8.5 \times 10 - 14$ erg cm$^{-2}$ s$^{-1}$ in the range 0.2–10 keV, excluding the flare) would translate into a luminosity of $5 \times 10^{30} < L_{\rm X} < 4 \times 10^{32}$ erg s$^{-1}$, which is too high for an active M-type star in 'quiescence' (see e.g. Stelzer et al. 2013).

An interesting possibility is the association of 3FGL J0838.8−2829 with the X-ray-variable source XMM J083850.4−282759, as a possible transitional millisecond pulsar (Archibald et al. 2009; Papitto et al. 2013). Such sources are often found in a subluminous disc state characterized by enhanced X-ray variability between a high and a low flux level that differ by a factor of ∼10, and often show occasional flaring activity on time-scales of several minutes (de Martino et al. 2013; Bogdanov et al. 2015), as we observe from XMM J083850.4−282759. A relatively bright emission is also observed at gamma-ray (de Martino et al. 2010; Stappers et al. 2014; Li et al. 2014), optical (de Martino et al. 2013; Bogdanov et al. 2015) and radio (Hill et al. 2011; Deller et al. 2015) wavelengths. Even though the absence of an ATCA radio detection from XMM J083850.4−282759 does not favour its identification as a transitional millisecond pulsar, the non-detection of a radio source might be compatible with a larger distance of the putative pulsar. In this respect, we note that the gamma-ray flux of 3FGL J0838.8−2829 (∼$10^{-9}$ ph cm$^{-2}$ s$^{-1}$ in the 1–100 GeV band; Acero et al. 2015), and its average X-ray flux (∼$8.5 \times 10^{-14}$ erg cm$^{-2}$ s$^{-1}$ in the 0.2–10 keV band) are ∼10 and 100 times smaller, respectively, than those observed from the prototypical transitional millisecond pulsar PSR J1023+0038, which is located at 1.4 kpc (Deller et al. 2012); hence, a larger distance would also be in line with other multiband source characteristics. Furthermore, the low spectral index and low level of variability of the GeV emission are

also in agreement with results for other binary millisecond pulsars observed by *Fermi*-LAT (Acero et al. 2015).

The detection of optical/near-infrared emission from a late-type companion star, as inferred from the observed colours, would suggest a redback system observed in the radio pulsar state. The constraints on the X-ray luminosity reported above would be in agreement with such a scenario. However, without knowing the orbital period, the strength of possible irradiation effects, the companion spectral type and the system distance, all the above considerations should be taken with some caution, and alternative scenarios (e.g. a black-widow system) cannot be ruled out.

## ACKNOWLEDGEMENTS

The scientific results reported in this article are based on observations obtained with *XMM–Newton* and *Swift*. *XMM–Newton* is an ESA science mission with instruments and contributions directly funded by ESA member states and the National Aeronautics and Space Administration (NASA). *Swift* is a NASA mission with the participation of the Italian Space Agency and the UK Space Agency. This research has made use of softwares and tools provided by the High Energy Astrophysics Science Archive Research Center (HEASARC), which is a service of the Astrophysics Science Division at NASA/GSFC and the High Energy Astrophysics Division of the Smithsonian Astrophysical Observatory. The research has also made use of data from the Two Micron All Sky Survey, which is a joint project of the University of Massachusetts and the Infrared Processing and Analysis Center/California Institute of Technology, funded by NASA and the National Science Foundation. We also made use of data products from the Wide-field Infrared Survey Explorer, which is a joint project of the University of California, Los Angeles, and the Jet Propulsion Laboratory/California Institute of Technology, funded by NASA. The CANICA project is funded by the CONACyT grant G28586-E (PI: Luis Carrasco). This research is based on observations collected at the European Organization for Astronomical Research in the Southern Hemisphere under ESO program 296.D-5034 (PI: Rea). The results reported in this article are also based on observations made by the Australia Telescope Compact Array (ATCA), which is part of the Australia Telescope National Facility that is funded by the Australian Government for operation as a National Facility managed by CSIRO. This article also uses observations made with the IAC80 operated on the island of Tenerife by the IAC in the Spanish Observatorio del Teide. We are grateful to the XMM-Newton, ESO and ATCA Directors for awarding us their proprietary Director's Time.

We thank Elisa Costantini for useful discussion, and gratefully acknowledge the referee for his/her useful comments and suggestions. NR, FCZ, PE and AB are supported by the NWO Vidi Grant A.2320.0076 and by the European COST Action MP1304 (NewCOMPSTAR). NR, FCZ, DFT, EdOW and JL are also supported by grants AYA2015-71042-P and SGR2014-1073. FCZ, DFT, AP, EB and CF acknowledge the International Space Science Institute (ISSI-Bern), which funded and hosted the international team 'The disc-magnetosphere interaction around transitional millisecond pulsars'. DdM acknowledges support from INAF–ASI I/037/12/0. AP acknowledges support via an EU Marie Skłodowska Curie fellowship under grant no. 660657-TMSP-H2020-MSCA-IF-2014. MH is supported by grants ESP2015-66134-R, SGR2014-1458 and FEDER funds. ML and JC acknowledge support by the Spanish grant AYA2013-42627. ML is also supported by EU's Horizon 2020 programme through a Marie Sklodowska-Curie Fellowship (grant no. 702638). JC also acknowledges support by the Leverhulme Trust through the Visiting Professorship Grant VP2-2015-046.

## REFERENCES

Acero F. et al., 2015, ApJS, 218, 23
Alpar M. A., Cheng A. F., Ruderman M. A., Shaham J., 1982, Nature, 300, 728
Anzolin G., de Martino D., Bonnet-Bidaud J.-M., Mouchet M., Gäpnsicke B. T., Matt G., Mukai K., 2008, A&A, 489, 1243
Archibald A. M. et al., 2009, Science, 324, 1411
Archibald A. M. et al., 2015, ApJ, 807, 62
Arnaud K. A., 1996, in Jacoby G. H., Barnes J., eds, Astronomy Society of the Pacific Conference Series Vol. 101, Astronomical Data Analysis Software and Systems V. Astron. Soc. Pac., San Francisco, p. 17
Bassa et al., 2014, MNRAS, 441, 1825
Bernardini F., de Martino D., Falanga M., Mukai K., Matt G., Bonnet-Bidaud J.-M., Masetti N., Mouchet M., 2012, A&A, 542, 22
Bernardini F. et al., 2013, MNRAS, 435, 2822
Blackburn J. K., 1995, in Shaw R. A., Payne H. E., Hayes J. J. E., eds, Astronomy Society of the Pacific Conference Series Vol. 77, Astronomical Data Analysis Software and Systems IV. Astron. Soc. Pac., San Francisco, p. 367
Bogdanov S. et al., 2015, ApJ, 806, 148
Boyd D. et al., 2014, Soc. Astron. Sci. Ann. Symp., 33, 163
Burrows D. N. et al., 2005, Space Sci. Rev., 120, 165
Campbell C. G., Schwope A. D., 1999, A&A, 343, 132
Coti Zelati F. et al., 2016, MNRAS, 456, 1913
Courvoisier T. J.-L. et al., 2003, A&A, 411, 53
Cropper M., 1990, Space Sci. Rev., 54, 195
De Luca A., Molendi S., 2004, A&A, 419, 837
de Martino D. et al., 2010, A&A, 515, A25
de Martino D. et al., 2013, A&A, 550, 89
de Martino D. et al., 2014, MNRAS, 444, 3004
Deller A. T. et al., 2012, ApJ, 756, L25
Deller A. T. et al., 2015, ApJ, 809, 13
den Herder J. W. et al., 2001, A&A, 365, L7
Ferrario L., de Martino D., Gänsicke B. T., 2015, Space Sci. Rev., 191, 111
Halpern J. P., Bogdanov S., Thorstensen J. R., 2017, ApJ, 838, 124
Harrison T. E., Campbell R. K., 2016, MNRAS, 459, 4161
Hill J. E. et al., 2004, in Flanagan K. A., Siegmund O. H. W., eds, Proc. SPIE Conf. Ser. Vol. 5165, X-Ray and Gamma-Ray Instrumentation for Astronomy XIII. SPIE, Bellingham, p. 217
Hill A. B. et al., 2011, MNRAS, 415, 235
Joshi A., Pandey J. C., Singh K. P., Agrawal P. C., 2016, ApJ, 830, 56
Lebrun F. et al., 2003, A&A, 411, 141
Li K. L., Kong A. K. H., Takata J., Cheng K. S., Tam P. H. T., Hui C. Y., Jin R., 2014, ApJ, 797, 111
Linares M., 2014, ApJ, 795, 72L
Lund N. et al., 2003, A&A, 411, 231
Masetti N. et al., 2013, A&A, 559, 58
Mason K. O. et al., 2001, A&A, 365, L36
Mauche C. W., Brickhouse N. S., Hoogerwerf R., Luna G. J. M., Mukai K., Sterken C., 2009, Inf. Bull. Var. Stars, 5876, 1
Mukai K., Hellier C., Madejski G., Patterson J., Skillman D. R., 2003, ApJ, 597, 479
Myers G. et al., 2017, PASP, 129, 4204
Norton A. J., Wynn G. A., Somerscales R. V., 2004, ApJ, 614, 349
Pagnotta A., Zurek D., 2016, MNRAS, 458, 1833
Papitto A., Torres D. F., 2015, ApJ, 807, 33
Papitto A. et al., 2013, Nature, 501, 517
Papitto A., Torres D. F., Li J., 2014, MNRAS, 438, 2105
Papitto A., de Martino D., Belloni T. M., Burgay M., Pellizzoni A., Possenti A., Torres D. F., 2015, MNRAS, 449, 26
Parker T. L., Norton A. J., Mukai K., 2005, A&A, 439, 213
Piirola V., Coyne G. V., Takalo S. J., Takalo L., Larsson S., Vilhu O., 1994, A&A, 283, 163

Predehl P., Schmitt J. H. M., 1995, A&A, 293, 889
Ramsay G., Cropper M., 2004, MNRAS, 2004, 347, 497
Ramsay G., Buckley David A. H., Cropper M., Harrop- Allin M. K., 1999, MNRAS, 303, 96
Rana V. R., Singh K. P., Barrett P. E., Buckley D. A. H., 2005, ApJ, 625, 351
Sault R. J., Teuben P. J., Wright M. C. H., 1995, in Shaw R. A., Payne H. E., Hayes J. J. E., eds, ASP Conf. Ser. Vol. 77, Astronomical Data Analysis Software and Systems IV. Astron. Soc. Pac., San Francisco, p. 433
Schwarz R., Schwope A. D., Staude A., Remillard R. A., 2005, A&A, 444, 213
Schwarz R., Schwope A. D., Staude A., Rau A., Hasinger G., Urrutia T., Motch C., 2007, A&A, 473, 511
Shafter A. W. et al., 2008, PASP, 120, 374
Silber A. D. et al., 1997, MNRAS, 290, 25
Stappers B. W. et al., 2014, ApJ, 790, 39
Staubert R. et al., 2003, A&A, 407, 987
Stelzer B., Marino A., Micela G., López-Santiago J., Liefke C., 2013, MNRAS, 431, 2063
Strüder L. et al., 2001, A&A, 365, 18
Takata J. et al., 2014, ApJ, 785, 131
Turner M. J. L. et al., 2001, A&A, 365, L27
Ubertini P. et al., 2003, A&A, 411, 131
Verner D. A., Ferland G. J., Korista K. T., Yakovlev D. G., 1996, ApJ, 465, 487
Warner B., 1995, Cataclysmic Variable Stars. Cambridge Univ. Press, Cambridge
Warner B., 2003, Cataclysmic Variable Stars. Cambridge Univ. Press, Cambridge, UK, p. 592
Willingale R., Starling R. L. C., Beardmore A. P., Tanvir N. R., O'Brien P. T., 2013, MNRAS, 431, 394
Wilms J., Allen A., McCray R., 2000, ApJ, 542, 914
Wright E. L. et al., 2010, AJ, 140, 1868
Wynn G. A., King A. R., 1992, MNRAS, 255, 83
Zdziarski A. A., Johnson W. N., Magdziarz P., 1996, MNRAS, 283, 193
Życki P. T., Done C., Smith D. A., 1999, MNRAS, 309, 561

## APPENDIX

During the referee process of this paper, a paper using our *XMM–Newton* data was published by Halpern, Bogdanov & Thorstensen (2017). In this Appendix we point out a few differences between the two publications.

(1) In our optical monitoring we could not detect any hint of periodicity in the optical monitoring of the transitional MSP candidate XMM J083850.4−282759, nor the broad minimum reported by Halpern et al. (2017), but we caution that the longest time series we collected span over about 2.9 h (about one half of the length of the Halpern et al. optical data set).

(2) Using our *XMM–Newton* data, these authors report a different modelling/interpretation of the X-ray light-curve. They assumed that a phase jump of $\sim$120° in the $\sim$1.6-h modulation occurs around the flux minimum and, using only the first part of the observations, derived a spin period of $\sim$1.58 h, which is barely compatible with our value. As for the orbital period, they measured it from radial velocities of H$\alpha$ in good-quality optical spectroscopic data and found $1.64 \pm 0.06$ h, in good agreement with our values. These differences result in a different interpretation of the nature of the mCV RX J0838−2827. In order to discern whether one description of the light-curve is to be preferred to the other, we analysed separately the *XMM–Newton* segments of data prior and after their suggested phase jump in both observations. The comparison was inconclusive, essentially because the orbital and spin periods derived in the two scenarios are almost identical and because not all subsets of data have enough frequency resolution to separate the $\Omega$ and $\omega$ peaks in the PSDs (see Fig. A1 for an example).

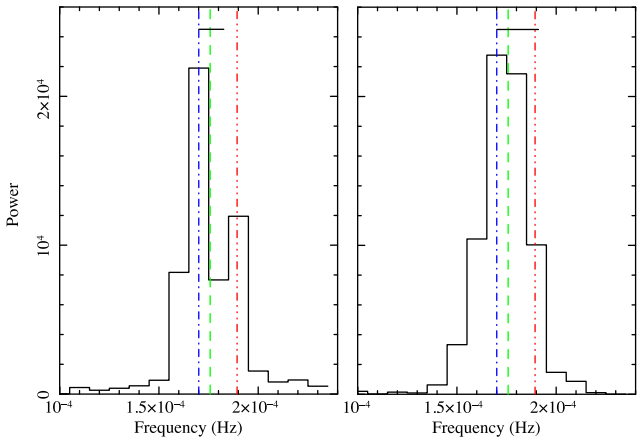


**Figure A1.** Zoom on the PSD structure around $\Omega$ (blue dot–dashed line) and $\omega$ (red three-dot–dashed line) in the second *XMM–Newton* observation (left) and only in the first 45 ks of it (right, before the flux minimum and the possible phase jump, see Section 5.1). The dashed green line indicates the frequency of the signal reported by Halpern et al. (2017). The length of the horizontal bar at the top indicates the Fourier intrinsic resolution of the data segment.

[1]*Institute of Space Sciences (IEEC–CSIC), Carrer de Can Magrans s/n, E-08193 Barcelona, Spain*
[2]*Anton Pannekoek Institute for Astronomy, University of Amsterdam, Postbus 94249, NL-1090-GE Amsterdam, The Netherlands*
[3]*Università dell' Insubria, via Valleggio 11, I-22100 Como, Italy*
[4]*INAF – Osservatorio Astronomico di Brera, via Bianchi 46, I-23807 Merate (LC), Italy*
[5]*INAF – Osservatorio Astronomico di Capodimonte, Salita Moiariello 16, I-80131 Napoli, Italy*
[6]*INAF – Osservatorio Astronomico di Roma, via Frascati 33, I-00078 Monteporzio Catone (RM), Italy*
[7]*Institució Catalana de Recerca i Estudis Avancats (ICREA), E-08010 Barcelona, Spain*
[8]*INAF – Istituto di Astrofisica Spaziale e Fisica Cosmica di Bologna, via Gobetti 101, I-40129 Bologna, Italy*
[9]*Departamento de Ciencias Fisicas, Universidad Andrés Bello, Fernández Concha 700, Las Condes, Santiago, Chile*
[10]*Instituto Nacional de Astrofisica Optica y Electronica (INAOE), Apartado Postal 51 y 216, 72000 Puebla, Mexico*
[11]*INAF – Osservatorio Astronomico di Cagliari, Via della Scienza 5, I-09047 Selargius (CA), Italy*
[12]*Australia Telescope National Facility, CSIRO Astronomy and Space Science, PO Box 76, Epping, NSW 1710, Australia*
[13]*ISDC, University of Geneva, chemin d'Écogia, 16 CH-1290 Versoix, Switzerland*
[14]*Instituto de Astrofísica de Canarias, c/ Vía Láctea s/n, E-38205 La Laguna, Tenerife, Spain*
[15]*Universidad de La Laguna, Dept. Astrofísica, E-38206 La Laguna, Tenerife, Spain*
[16]*Departament de Física, EEBE, Universitat Politècnica de Catalunya, c/ Eduard Maristany 10, E-08019 Barcelona, Spain*
[17]*Max-Planck-Institut für Radioastronomie, Auf dem Hügel 69, D-53121 Bonn, Germany*
[18]*Argelander-Institute für Astronomie, Universität Bonn, Auf dem Hügel 71, D-53121 Bonn, Germany*
[19]*Department of Physics, Astrophysics, University of Oxford, Denys Wilkinson Building, Keble Road, Oxford OX1 3RH*

This paper has been typeset from a TEX/LATEX file prepared by the author.